

# Topological Transitions Enhance the Performance of Twisted Thermophotovoltaic Systems

Rongqian Wang,<sup>1</sup> Jincheng Lu<sup>2</sup>, Xiaohu Wu<sup>3,\*</sup>, Jiebin Peng,<sup>4,†</sup> and Jian-Hua Jiang<sup>1,‡</sup>

<sup>1</sup>*Institute of Theoretical and Applied Physics, School of Physical Science and Technology, and Collaborative Innovation Center of Suzhou Nano Science and Technology, Soochow University, Suzhou 215006, China*

<sup>2</sup>*Jiangsu Key Laboratory of Micro and Nano Heat Fluid Flow Technology and Energy Application, School of Physical Science and Technology, Suzhou University of Science and Technology, Suzhou 215009, China*

<sup>3</sup>*Shandong Institute of Advanced Technology, Jinan 250100, China*

<sup>4</sup>*School of Physics and Optoelectronic Engineering, Guangdong University of Technology, Guangzhou, Guangdong Province 510006, China*

(Received 5 August 2022; revised 28 February 2023; accepted 10 March 2023; published 18 April 2023)

Twisted bilayer two-dimensional electronic systems give rise to many exotic phenomena and unveil a new frontier for the study of quantum materials. In photonics, twisted two-dimensional systems coupled via near-field interactions offer a platform to study localization and lasing. Here, we theoretically propose that twisting can be an unprecedented tool to tune the performance of near-field thermophotovoltaic systems. Remarkably, through twisting-induced photonic topological transitions, we achieve significant tuning of the thermophotovoltaic energy efficiency and power. The underlying mechanism is related to the change of the photonic isofrequency contours from elliptical to hyperbolic geometries in a setup where the hexagonal-boron-nitride metasurface serves as the heat source and the indium-antimonide *p-n* junction serves as the cell. We find that a notably high energy efficiency, nearly 53% of the Carnot efficiency, can be achieved in our thermophotovoltaic system, while the output power can reach up to  $1.1 \times 10^4 \text{ W/m}^2$  without requiring a large temperature difference between the source and the cell. Our results indicate the promising future of twisted near-field thermophotovoltaics and paves the way towards tunable, high-performance thermophotovoltaics and infrared detection.

DOI: 10.1103/PhysRevApplied.19.044050

## I. INTRODUCTION

As a solid-state renewable energy resource, thermophotovoltaic (TPV) systems have shown great potential in a wide range of applications, including solar energy utilization and waste heat recovery [1–3]. The photovoltaic cell, which is separated from a thermal emitter by a vacuum gap in a TPV system, can absorb the thermal radiation from the emitter and convert heat into electrical energy via the photovoltaic effect [4,5]. As the power densities of far-field TPV systems are fundamentally constrained by the Stefan-Boltzmann law, near-field effects are explored to break the black-body limit [6–9]. By reducing the vacuum gap to be comparable with or smaller than the characteristic thermal wavelength, the power densities in near-field TPV (NTPV) systems can far exceed those in far-field systems through strong near-field coupling. The numerical

and experimental investigations of NTPV systems have attracted extensive attention in recent decades [10–20].

To effectively match the gap frequency of the photovoltaic cell to the emission spectrum of the emitter, one can exploit the coupling of surface polaritons, e.g., surface-plasmon polaritons [21,22], surface-phonon polaritons (SPhPs) [23,24], and magnetoplasmon polaritons [25,26]. Various types of surface polaritons have been studied extensively and have demonstrated their ability to enhance the near-field thermal radiation and to improve the performance of NTPV systems [10,27–33]. Moreover, it has been shown that near-field radiative heat transfer can be greatly enhanced by the hybridization effect of polaritons. In particular, the surface-plasmon polaritons in graphene can couple with the SPhPs in hexagonal boron nitride (*h*-BN) films to form hybrid polaritons that assist photon tunneling [34–36]. Recently, inspired by the pioneering work of Hu *et al.*, heat transfer based on twisted hyperbolic systems has been explored [37,38]. The emitter and absorber in these systems are made by a uniaxial hyperbolic metasurface and can support several types of anisotropic hyperbolic polaritons. By manipulating the

\*xiaohu.wu@iat.cn

†pengjiebin@hotmail.com

‡jianhujiang@suda.edu.cn

twist angle between the emitter and the absorber, topological transitions can be induced in the dispersion of the polaritons, resulting in enhancement of the radiative heat transfer [39,40]. Existing studies on near-field thermal management via twist are restricted to radiative heat transfer; however, a primary concern of topological transitions with the NTPV systems is still missing.

The high performance of NTPV systems is limited due to the challenges in creating selective thermal emitters with large emittance for photon energies larger than the band-gap energy of the photovoltaic cell and creating photovoltaic cells with perfect absorption of the above-gap thermal radiation [41–43]. In our previous works, we designed and optimized graphene-*h*-BN-indium-antimonide (InSb) near-field structures to enhance the performance of NTPV systems working in the temperature range of common industrial waste heat (400 to 800 K) [44,45]. When a thin *h*-BN flake is patterned into a metasurface structure, the two permittivities along the direction perpendicular to the optical axis become anisotropic [43,46]. In-plane hyperbolicity arises in *h*-BN metasurfaces when the real parts of the two permittivities have different signs, which supports highly confined in-plane hyperbolic phonon polaritons. Such anisotropic polaritons give rise to the enhancement of the photonic local density of states (PLDOS) around the synthetic transverse optical (STO) phonon frequency and enable good near-field matching of polaritons above the gap frequency in InSb [43].

In this work, we theoretically propose to use the *h*-BN metasurface to act as a selective near-field emitter and narrow-band-gap InSb *p-n* junction with an *h*-BN metasurface as an effective TPV cell and examine the effects of twists in both the in-plane and out-of-plane directions on the performance of NTPV systems. By twisting the optical axis of the *h*-BN metasurface to the *y* direction, we demonstrate that the out-of-plane topological transitions of the dispersion of SPhPs enables the suppression of the excitation of the SPhPs, which reduces the below-gap radiative heat transfer between the emitter and the cell [47–49]. By manipulating the twist angle between the two *h*-BN metasurfaces, we show that the in-plane topological transitions further affect the output power and energy conversion efficiency of the proposed system. The performance of the proposed system is significantly enhanced without maintaining a large temperature difference between the source and the cell, which provides an achievable solution to a technical challenge in existing experiments [14–20]. Unlike solar cells, the NTPV systems proposed here are designed to harvest energy for small temperature differences not far away from ambient temperature. The applications of this type of device can be wearable waste heat harvesting or other portable small energy converters instead of large-scale industrial-level energy generators.

This work is structured as follows. In Sec. II, we design an NTPV system and clarify the radiative heat flux exchanged between the emitter and the cell. We study the photon transmission coefficient to elucidate the out-of-plane and in-plane topological transitions in the proposed NTPV system. In Sec. III, We examine the effects of both the in- and out-of-plane twists on the performance of the NTPV system. We analyze the spectral distributions of the photoinduced current density and incident heat flux. Finally, we summarize and conclude in Sec. IV.

## II. NEAR-FIELD THERMAL RADIATION AND TWIST-INDUCED TOPOLOGICAL TRANSITION

### A. Near-field thermal radiation

The proposed NTPV system is illustrated by Fig. 1(a), where the near-field emitter with temperature  $T_{\text{emit}}$  and the cell with temperature  $T_{\text{cell}}$  are separated by a vacuum gap with distance  $d$ . The emitter is an *h*-BN metasurface with thickness  $t_{\text{BN}}$ , which consists of a periodic array of *h*-BN nanoribbons. The periodicity and stripe width of the nanoribbons are  $p$  and  $w$ , respectively. The TPV cell is made of an InSb *p-n* junction, which is coated by an *h*-BN metasurface identical to that on the emitter. In this NTPV system, in-plane hyperbolic phonon polaritons induced by the in-plane anisotropy of the *h*-BN metasurface are excited to enhance the near-field coupling between the emitter and the cell. The optical property of the *h*-BN metasurface is described by the effective permittivity, where the effective anisotropic permittivity tensor  $\boldsymbol{\epsilon}_{\text{eff}}$  components are described by a modified effective-medium model (optical axis in the *z* direction) [41–43]:

$$\begin{aligned}\epsilon_{\text{eff},x} &= \left( \frac{1-\xi}{\epsilon_{\perp}} + \frac{\xi}{\epsilon_c} \right)^{-1}, \\ \epsilon_{\text{eff},y} &= (1-\xi)\epsilon_{\perp} + \xi\epsilon_{\text{air}}, \\ \epsilon_{\text{eff},z} &= (1-\xi)\epsilon_{\parallel} + \xi\epsilon_{\text{air}}.\end{aligned}\quad (1)$$

Here  $\xi = (p-w)/p$  is the filling factor;  $\epsilon_c = [2p/(\pi t_{\text{BN}})] \ln[\csc(\frac{1}{2}\pi\xi)]$  is a nonlocal correction parameter taking into account the near-field coupling of adjacent ribbons and the corresponding nonlocality [41–43];  $\epsilon_{\perp}$  and  $\epsilon_{\parallel}$  are the in-plane and out-of-plane permittivities of *h*-BN, respectively [50–52]; and  $\boldsymbol{\epsilon}_{\text{eff}}$  is a diagonal matrix, with  $\epsilon_{\text{eff},x}$ ,  $\epsilon_{\text{eff},y}$ , and  $\epsilon_{\text{eff},z}$ . The validity of the modified effective-medium theory is corroborated by the simulation of the PLDOS using a genuine grating structure [43,51,53]. For convenience, we define two kinds of angles: the out-of-plane twist angle  $\varphi$  denotes the angle between the *z* direction and the optical axis of *h*-BN and describes the rotation of the optical axis in the *y-z* plane; and the in-plane twist angle  $\theta$  denotes the angle between two parallel *h*-BN metasurfaces and describes the relative rotation in the *x-y* plane.

The exchanged radiative heat flux between the emitter and the cell can be calculated based on fluctuational electrodynamics [54,55]:

$$\begin{aligned} Q_{\text{rad}}(T_{\text{emit}}, T_{\text{cell}}, \omega, \Delta\mu) &= \frac{\Theta_1(T_{\text{emit}}, \omega)}{4\pi^2} \int_0^{2\pi} \int_0^\infty \zeta(\omega, k, \phi) k dk d\phi \\ &\quad - \frac{\Theta_2(T_{\text{cell}}, \omega, \Delta\mu)}{4\pi^2} \int_0^{2\pi} \int_0^\infty \zeta(\omega, k, \phi) k dk d\phi. \end{aligned} \quad (2)$$

Here  $\Theta_1(T_{\text{emit}}, \omega) = \hbar\omega / [\exp(\hbar\omega/k_B T_{\text{emit}}) - 1]$  and  $\Theta_2(T_{\text{cell}}, \omega, \Delta\mu) = \hbar\omega / [\exp[(\hbar\omega - \Delta\mu)/k_B T_{\text{cell}}] - 1]$  are the Planck mean oscillator energies of a black body at temperature  $T_{\text{emit}}$  and  $T_{\text{cell}}$ , respectively;  $\Delta\mu$  is the electrochemical potential difference across the *p-n* junction for  $\omega > \omega_{\text{gap}}$ , and  $\phi$  is the azimuthal angle. Finally,  $\zeta(\omega, k, \phi)$  is the photon transmission coefficient which describes the probability of photons tunneling across the vacuum gap, which can be expressed as [48]

$$\zeta(\omega, k, \phi) = \begin{cases} \text{Tr}[(\mathbf{I} - \mathbf{R}_{\text{cell}}^\dagger \mathbf{R}_{\text{cell}} - \mathbf{T}_{\text{cell}}^\dagger \mathbf{T}_{\text{cell}}) \mathbf{D} (\mathbf{I} - \mathbf{R}_{\text{emit}}^\dagger \mathbf{R}_{\text{emit}} - \mathbf{T}_{\text{emit}}^\dagger \mathbf{T}_{\text{emit}}) \mathbf{D}^\dagger], & k < k_0, \\ \text{Tr}[(\mathbf{R}_{\text{cell}}^\dagger - \mathbf{R}_{\text{cell}}) \mathbf{D} (\mathbf{R}_{\text{emit}} - \mathbf{R}_{\text{emit}}^\dagger) \mathbf{D}^\dagger] e^{-2|k_z|d}, & k > k_0. \end{cases} \quad (3)$$

Here  $k_0 = \omega/c$  is the wave-vector in vacuum with  $c$  the speed of light in vacuum;  $k = \sqrt{k_x^2 + k_y^2}$  and  $k_z = \sqrt{k_0^2 - k^2}$  are the wave-vector components parallel and perpendicular to the  $x$ - $y$  plane in vacuum, respectively; and  $k_x$  and  $k_y$  are the wave-vector components along the  $x$  axis and  $y$  axis, respectively. Note that  $\text{Tr}(\cdot)$  takes the trace of a matrix; “ $\dagger$ ” denotes conjugate transpose;  $\mathbf{I}$  is a  $2 \times 2$  unit matrix;  $\mathbf{D} = (\mathbf{I} - \mathbf{R}_{\text{emit}} \mathbf{R}_{\text{cell}} e^{2ik_z d})^{-1}$  is the Fabry-Pérot-like denominator matrix describing the multiple scattering between the two interfaces of the emitter and the cell; and  $\mathbf{R}_j$  and  $\mathbf{T}_j$  ( $j = \text{emit, cell}$ ) are the reflection and transmission coefficient matrices at the interface between the emitter (cell) and the air, respectively. These last two coefficients can be obtained using a modified  $4 \times 4$  transfer matrix method [26,48]. The validity of this method has been verified by some experiments based on actual hyperbolic materials [56,57]. Detailed calculations of the coefficients can be found in Appendix A.

The permittivities of *h*-BN and the proposed *h*-BN metasurfaces are presented in Fig. 1(b). As shown in the upper panel, the in-plane permittivity  $\varepsilon_{\perp}$  is negative in the frequency range from  $1.5 \times 10^{14}$  to  $1.6 \times 10^{14}$  rad/s; the out-of-plane permittivity  $\varepsilon_{\parallel}$  is negative in the range of  $2.58 \times 10^{14}$  to  $3.03 \times 10^{14}$  rad/s for natural *h*-BN. The negativeness of the permittivities defines two frequency regions with strong light-matter interaction, respectively termed as type I and type II hyperbolic regions. The rest-strahlen effects occurring in these two regions lead to strong reflection and suppressed transmission, which are crucial for the enhancement of near-field thermal radiation [44].

In the lower panel of Fig. 1(b), we observe that a significant difference between the in-plane permittivities  $\varepsilon_{\text{eff},x}$  and

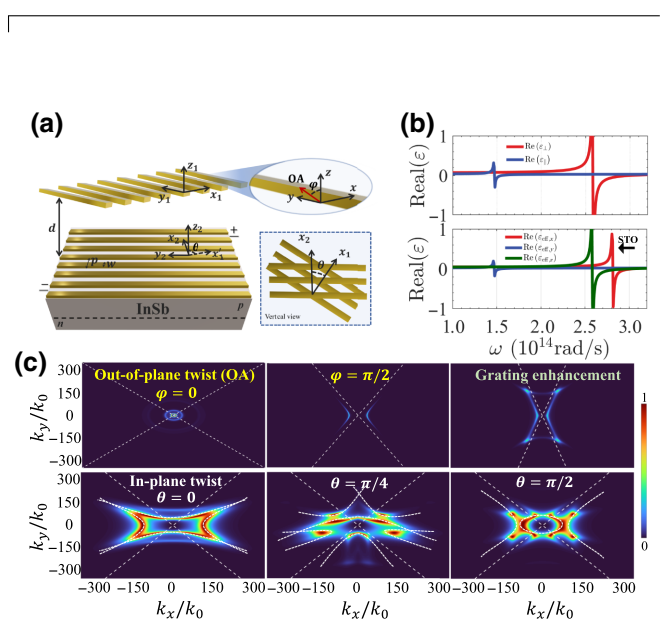


FIG. 1. (a) Schematic illustration of the NTPV system. The near-field emitter of temperature  $T_{\text{emit}}$  is an *h*-BN metasurface based on a grating made of nanoribbons, whose periodicity and stripe width are  $p$  and  $w$ , respectively. The cell of temperature  $T_{\text{cell}}$  is an InSb *p-n* junction coated by a metasurface identical to that on the emitter. The distance between the emitter and the cell is set as  $d$ . The temperature of the *h*-BN metasurface attached to the InSb cell has the same temperature as the InSb cell. The twist angle between the main axes of the two gratings is  $\theta$ . The upper inset shows that the optical axis of *h*-BN is in the  $x$ - $z$  plane and is tilted off the  $z$  axis by an angle  $\varphi$ . The lower inset shows a top view of the twisted hyperbolic system at a rotation angle  $\theta$  with respect to the  $x$  axis. (b) Upper panel: real parts of the in-plane and out-of-plane permittivities of the *h*-BN. Lower panel: real parts of the permittivities along the three principal axes of the *h*-BN metasurface. (c) The topological transitions induced by the out-of-plane (upper panels) and in-plane (lower panels) twists.

$\varepsilon_{\text{eff},y}$  is conspicuous when the  $h$ -BN layer is patterned into a metasurface structure. For  $h$ -BN constructed as a metasurface, the STO resonance at  $\omega = 2.78 \times 10^{14}$  rad/s emerges in the middle of the upper reststrahlen band, which originates from the strong collective near-field coupling of the dipolar phonon polariton resonance of the individual  $h$ -BN ribbons [43]. The emergence of the STO resonance brings about an extra hyperbolic band (with  $\varepsilon_{\text{eff},y} > 0$  and  $\varepsilon_{\text{eff},x} < 0$ ), as indicated by the red solid line in Fig. 1(b). Because of the STO, the PLDOS on the metasurface differs dramatically from that of the natural  $h$ -BN. As demonstrated in Ref. [43], the  $h$ -BN thin film only exhibits one PLDOS peak within the reststrahlen band while the metasurface exhibits two PLDOS peaks located on either side of the STO frequency. Since a high PLDOS indicates strong anisotropic phonon polaritons, which are efficient carriers in near-field tunneling, the  $h$ -BN metasurface may serve as a robust near-field emitter for the NTPV system.

## B. Twist-induced topological transition

To demonstrate the physical mechanisms of twist-induced topological transition in an NTPV system, Fig. 1(c) examines the photon transmission coefficient  $\zeta$  in the  $k_x$ - $k_y$  plane with fixed frequency  $\omega$ . The upper and lower panels show the out-of-plane and in-plane twist-induced topological transitions, respectively. The bright branches indicate high photon transmission and the dashed lines are the numerical solution of the implicit function about the Fabry-Pérot-like denominator matrix  $\mathbf{D}$ , i.e.,  $\text{Tr}(\mathbf{D}^{-1}) = 0$ .

With the optical axis lying in the  $z$  direction [upper panel of Fig. 1(c)], the energy transmission coefficient exhibits rotational symmetry in the  $k_x$ - $k_y$  plane arising from the in-plane isotropy of  $h$ -BN, which indicates the contribution of elliptical surface phonon polaritons (ESPhPs). The ESPhPs supported by the  $h$ -BN thin films are excited and contribute to the photon tunneling between the emitter and the cell. After twisting the optical axis to the  $y$  direction, the photon transmission coefficient becomes hyperbolic due to the in-plane anisotropy. It is demonstrated that hyperbolic surface phonon polaritons (HSPhPs) are excited after optical axis twisting and there is an out-of-plane twist-induced topological transition. In addition, owing to the emergence of the new hyperbolic band through the construction of the grating metasurface, more high- $k$  HSPhPs can be excited and thus enhance the photon transmission.

The lower panel of Fig. 1(c) presents another in-plane twist-induced topological transition at resonance frequency: when the twist angle  $\theta$  between the two metasurfaces changes from zero to  $\pi/2$ , the bright branch of the photon transmission coefficient changes markedly from hyperbolic (open) to elliptical (closed). We also find that there are band splitting (from 0 to  $\pi/4$ ) and band degeneracy (from  $\pi/4$  to  $\pi/2$ ) due to the  $\theta$ -dependent near-field

coupling. Meanwhile, the excitation of the high- $k$  HSPhPs is suppressed, and the low- $k$  ESPhPs dominate the photon tunneling, resulting in the reduction of radiative heat flux.

To show the tuning effects of the twist-induced topological transitions in the NTPV system, Fig. 2 investigates the photon transmission coefficients as functions of angular frequency  $\omega$  and in-plane wave-vector  $k$  plane. For convenience, we select three significant modes in the enhanced transmission for these systems, respectively denoted by modes ①, ②, and ③. Figure 2(a) shows that the photon transmission is enhanced in the two hyperbolic regions of  $h$ -BN. The enhanced transmission below the gap frequency of the InSb  $p$ - $n$  junction (mode ①, about  $1.55 \times 10^{14}$  rad/s) is due to the strong coupling of the ESPhPs supported by the  $h$ -BN thin films of the emitter and the cell. The high transmission above the gap frequency of the InSb  $p$ - $n$  junction (mode ②, about  $2.62 \times 10^{14}$  rad/s, and mode ③, about  $2.81 \times 10^{14}$  rad/s) originates from the resonant coupling between the ESPhPs in  $h$ -BN and the electron-hole excitations in the InSb  $p$ - $n$  junction.

As shown in Fig. 2(b), there are three salient features of topological transition caused by the twist of the optical axis: (i) the below-gap ESPhPs (mode ①,  $\approx 1.55 \times 10^{14}$  rad/s) are significantly weakened; (ii) one above-gap transmission mode (②,  $\approx 2.73 \times 10^{14}$  rad/s) can be transformed from ESPhPs to HESPhPs with reduced transmission probability and wave-vector range  $k_{\text{max}} < 100k_0$ ; and (iii) other ESPhPs (mode ③,  $\approx 2.99 \times 10^{14}$  rad/s) have emerged due to the in-plane anisotropy. Because of the strong coupling of the emerged ESPhPs between the emitter and the cell, the photon transmission around this mode is much enhanced compared to the case in Fig. 2(a), with increased transmission probability and wave-vector range  $k_{\text{max}} \approx 180k_0$ . These results are consistent with Ref. [48].

The near-field coupling between HSPhPs and emerged ESPhPs can be enhanced by grating effects. For mode ② (about  $2.83 \times 10^{14}$  rad/s), the in-plane hyperbolic dispersion ( $\varepsilon_x = -47.9263 + 14.5097i$ ,  $\varepsilon_y = 0.0003 + 0.1102i$ ) is formed by near-field coupling of the phonon polaritons in individual  $h$ -BN nanoribbons [43]. For mode ③ (about  $2.96 \times 10^{14}$  rad/s), there is an elliptical in-plane dispersion with  $\varepsilon_x = -2.1815 + 0.2079i$  and  $\varepsilon_y = -2.0932 + 0.0002i$  for the phonon polaritons. As presented in Fig. 2(c), when the  $h$ -BN thin film is patterned into a metasurface structure (with  $p = 100$  nm,  $\xi = 0.4$ ), the above-gap HSPhPs (mode ②,  $\approx 2.83 \times 10^{14}$  rad/s) and emerged ESPhPs (mode ③,  $\approx 2.96 \times 10^{14}$  rad/s) of the NTPV system are further hybridized and form a strong resonant mode in the high- $k$  region. From the viewpoint of topological transition, we find that the resonant mode can form a flat band in the  $k_x$  -  $k_y$  plane, i.e., transition modes between ESPhPs and HSPhPs, and the PLDOS can be significantly enhanced in the resonant (flat-band) condition. Originating from the strong collective near-field coupling

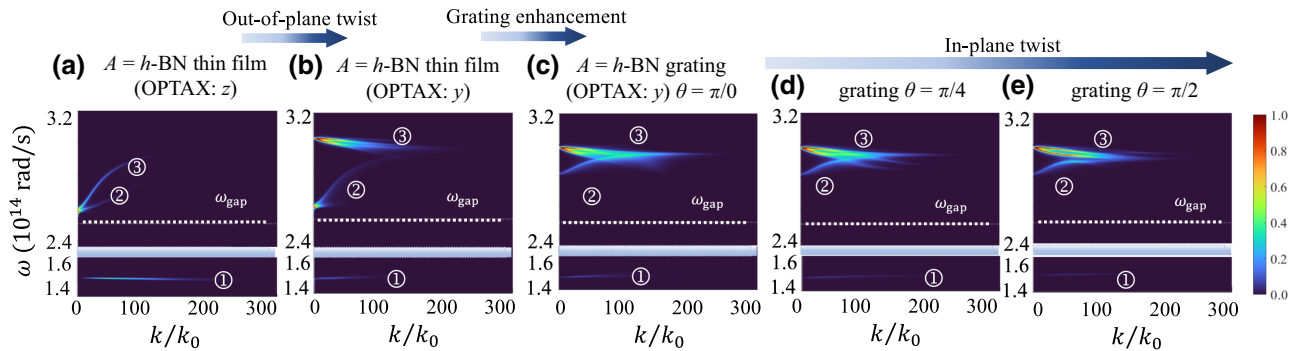


FIG. 2. The photon transmission coefficient  $\zeta$  as functions of  $\omega$  and  $k$ . (a),(b) Out-of-plane twist on the photon transmissions of NTPV systems. (c)–(e) In-plane twist on the NTPV system based on  $h$ -BN gratings. Parameters: the thickness of both the  $h$ -BN thin film and metasurface is  $t_{\text{BN}} = 10$  nm; the periodicity and the filling factor of the  $h$ -BN metasurface are  $p = 100$  nm and  $\xi = 0.4$ , respectively. The temperatures of the emitter and the cell are set at  $T_{\text{emit}} = 450$  K and  $T_{\text{cell}} = 320$  K, respectively. The vacuum gap distance is  $d = 20$  nm.

(negative  $\varepsilon_x$ ) of individual nanoresonators (Fabry-Pérot polariton resonances at nanoribbons), the ESPhPs and HSPhPs are both excited and contribute to the enhanced transmission.

As demonstrated in Figs. 2(c)–2(e), we move to the dependence of in-plane twist on photon transmission  $\zeta$ , including both below the gap ( $\omega < \omega_{\text{gap}}$ ) and above the gap ( $\omega > \omega_{\text{gap}}$ ). Because of the suppression of the HSPhPs induced by the in-plane topological transition, the photon transmission at the coupling mode between modes ② and ③ becomes weakened and shrinks to a narrower wave-vector region when the twist angle  $\theta$  changes from 0 to  $\pi/2$ . While, for mode ①, the transmission is slightly enhanced when  $\theta = \pi/4$  but suppressed for the twist angle increasing to  $\pi/2$ . From the above spectral analysis, we numerically show an enhancement of photon transmission coefficients through the adjustment of in-plane and out-of-plane twisting. The effects of the near-field couplings on the NTPV systems are elaborated in the following. For further discussion on the contribution of the three resonant modes, please refer to Appendix B.

### III. THE TOPOLOGICAL TRANSITIONS ON NTPV SYSTEMS

Based on the detailed balance analysis, the actual electric current density  $I_e$  of the TPV cell is derived as [58]

$$I_e = (I_{\text{ph}} - I_0[\exp(eV/k_B T_{\text{cell}}) - 1])\eta_{\text{QE}} \equiv I_{e,\text{max}}\eta_{\text{QE}}, \quad (4)$$

where  $V = \Delta\mu/e$  is the operating voltage of the cell [58],  $I_{e,\text{max}}$  is the maximum electric current density, and  $\eta_{\text{QE}}$  is the mean quantum efficiency [1]. Here, we consider the ideal situation, i.e.,  $\eta_{\text{QE}} = 100\%$ . Also here,  $I_0$  is the reverse saturation current density [59], whereas  $I_{\text{ph}}$  is the photogeneration current density, which arises from the radiation absorption of the cell in the frequency range

above the band gap

$$I_{\text{ph}} = e \int_{\omega_{\text{gap}}}^{\infty} \frac{Q_{\text{rad}}(T_{\text{emit}}, T_{\text{cell}}, \omega, \Delta\mu)}{\hbar\omega} d\omega. \quad (5)$$

The output electric power density  $P_e$  of the NTPV system is defined as the product of the net electric current density and the voltage bias,

$$P_e = -I_e V, \quad (6)$$

and the incident radiative heat flux is given by the integral of the radiative heat flux defined in Eq. (2):

$$\begin{aligned} Q_{\text{inc}} &= \int_0^{\infty} Q_{\text{rad}}(T_{\text{emit}}, T_{\text{cell}}, \omega, \Delta\mu) d\omega \\ &= \int_0^{\infty} \frac{d\omega}{(2\pi)^3} \Theta_1(T_{\text{emit}}, \omega) \int_0^{2\pi} \int_0^{\infty} \zeta(\omega, k, \phi) k dk d\phi \\ &\quad - \int_{\omega_{\text{gap}}}^{\infty} \frac{d\omega}{(2\pi)^3} \Theta_2(T_{\text{cell}}, \omega, \Delta\mu) \\ &\quad \times \int_0^{2\pi} \int_0^{\infty} \zeta(\omega, k, \phi) k dk d\phi \\ &\quad - \int_0^{\omega_{\text{gap}}} \frac{d\omega}{(2\pi)^3} \Theta_1(T_{\text{cell}}, \omega) \\ &\quad \times \int_0^{2\pi} \int_0^{\infty} \zeta(\omega, k, \phi) k dk d\phi. \end{aligned} \quad (7)$$

The integrand functions of frequency in Eqs. (5) and (7) are defined as the spectral functions  $Q_{\text{rad}}(\omega)$  and  $I_{\text{ph}}(\omega)$ , respectively. The energy efficiency  $\eta$  is given by the ratio between the output electrical power density  $P_e$  and the

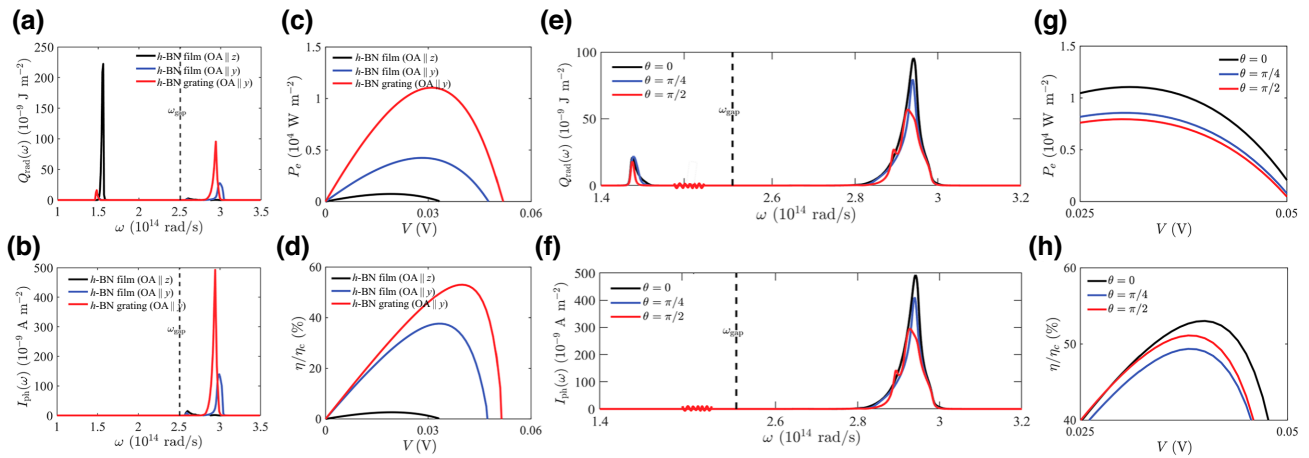


FIG. 3. (a)–(d) Effects of out-of-plane twist on the performance of NTPV systems. (a) Radiative heat spectra  $Q_{\text{rad}}(\omega)$  and (b) photoinduced current spectra  $I_{\text{ph}}(\omega)$  for the  $A$ - $A$ -InSb NTPV systems ( $A = h$ -BN thin film or  $h$ -BN grating metasurface) as a function of  $\omega$ , where the voltage bias  $V$  is at maximum output power for each set-up. (c) Electrical power density  $P_e$  and (d) energy conversion efficiency  $\eta/\eta_C$  in units of the Carnot efficiency ( $\eta_C$ ) of the  $A$ - $A$ -InSb NTPV systems as a function of voltage bias  $V$ . (e)–(h) Effects of in-plane twist on the performance of NTPV systems: (e)  $Q_{\text{rad}}(\omega)$  and (f)  $I_{\text{ph}}(\omega)$  for the NTPV system based on  $h$ -BN gratings as a function of  $\omega$  at different twisting angles  $\theta$ , where  $V = 0.03$  V; (g)  $P_e$  and (h)  $\eta/\eta_C$  for the NTPV system based on  $h$ -BN gratings as a function of voltage bias  $V$  at different twisting angles  $\theta$ . Parameters:  $T_{\text{emit}} = 450$  K,  $T_{\text{cell}} = 320$  K,  $d = 20$  nm,  $t_{\text{BN}} = 10$  nm,  $p = 100$  nm, and  $\xi = 0.4$ .

incident radiative heat flux  $Q_{\text{inc}}$  [46],

$$\eta = \frac{P_e}{Q_{\text{inc}}}. \quad (8)$$

Figures 3(a) and 3(b) reveal the spectral functions  $Q_{\text{rad}}(\omega)$  and  $I_{\text{ph}}(\omega)$  of the three different NTPV systems, i.e.,  $h$ -BN film with optical axis parallel to the  $z$  axis (black line),  $h$ -BN film with twisted optical axis parallel to the  $y$  axis (blue line), and  $h$ -BN grating with twisted optical axis parallel to the  $y$  axis (red line). All three lines in Fig. 3(a) show that the radiative heat spectrum  $Q_{\text{rad}}(\omega)$  is strengthened in the two hyperbolic bands of  $h$ -BN for all three NTPV systems. But the black line shows that the incident heat spectrum below the gap frequency of InSb is much higher than that above it for the  $h$ -BN thin film without a twisted optical axis. When the optical axis is twisted by  $\pi/2$  into the  $y$  direction (the two  $A$ - $A$ -InSb NTPV systems with  $A = h$ -BN thin film and  $A = h$ -BN grating), this high heat spectrum decreases dramatically due to the suppression of ESPHPs caused by the twist of the optical axis. A similar phenomenon has been studied in Ref. [48]. For the system with  $h$ -BN thin film (with the optical axis in the  $y$  direction), the incident heat spectrum above the gap frequency  $\omega_{\text{gap}}$  is enhanced predominantly compared with that below it, with the success attributed to the topological transition of ESPHPs to HSPHPs and the emerged ESPHP modes. For the NTPV system with  $A = h$ -BN metasurface, due to the strong coupling between ESPHPs and HSPHPs, a higher incident heat spectrum is exhibited above the gap frequency of InSb. Consistent with the incident heat

spectrum, the photon-induced current of the system with  $A = h$ -BN metasurface is much larger than that of the other two systems with  $h$ -BN thin films.

Indeed, from Eq. (5), it is clear that finding *only* the contribution from above the band gap, i.e.,  $\omega > \omega_{\text{gap}}$ , can improve the performance of NTPV cells [60]. In contrast, enhancement below the band gap leads to reduced energy efficiency, since these photons are useless for energy conversion. The high transmission region above the band gap is mainly due to the resonant coupling between the ESPHPs (HSPHPs) and the electron-hole excitation in the InSb junction. The system with  $A = h$ -BN grating possesses significantly increased above-gap incident heat spectrum and dramatically decreased below-gap spectrum, as shown in Figs. 3(a) and 3(b). This finally brings about the excellent performance of the system with  $A = h$ -BN grating, with the highest output power of about  $1.1 \times 10^4 \text{ W/m}^2$  and an energy efficiency of nearly 53 of the Carnot efficiency  $\eta_C$  [see Figs. 3(c) and 3(d)]. On the contrary, the highest incident heat spectrum below the band gap and the lowest heat spectrum above the band gap lead to the lowest energy efficiency and output power of the system with  $A = h$ -BN thin film (with optical axis in the  $z$  direction) [see the black solid line in Figs. 3(c) and 3(d)]. The moderate performance in the system with  $A = h$ -BN thin film (with optical axis in the  $y$  direction) originates from the enhanced above-gap incident heat spectrum and decreased below-gap spectrum compared to that of the system with  $A = h$ -BN thin film (with optical axis in the  $z$  direction).

Eventually, we turn to investigate the effects of the in-plane twist on the performances of the NTPV system based

on  $h$ -BN gratings [Figs. 3(e)–3(h)]. It is evident that the radiative heat spectrum  $Q_{\text{rad}}$  above the gap decreases with larger twist angle  $\theta$  [in Fig. 3(e)], so that it leads to the reduction of the photoinduced current spectral functions using Eq. (5) [see Fig. 3(f)], which is consistent with the previous analysis.

At this point, it becomes transparent that the optimal electric output power and efficiency of the NTPV system without an in-plane twist are much better than those with a twist. The NTPV system without a twist benefits from the narrowband nature of photon absorption, which gives rise to improved energy efficiency as compared with broadband photon absorption, as proved in Ref. [61]. Here we have to point out that, for the below-gap heat spectrum, the energy efficiency exhibits a nonmonotonic dependence versus the twisting angle  $\theta$ . According to Eq. (8), the reduced power divided by the increased incident radiation ultimately leads to reduced efficiency (about 49 of  $\eta_C$ ) for  $\theta = \pi/4$ . Likewise, the reduction of output power and input radiation contemporaneously produces a moderate efficiency for  $\theta = \pi/2$ .

#### IV. SUMMARY AND OUTLOOK

In this work, we propose an NTPV system based on  $A = h$ -BN gratings where twisting triggers dramatic changes in the optical properties. In particular, the below-absorption-gap (wasted) radiative heat transfer can be suppressed by twisting the optical axis of  $h$ -BN into the  $y$  axis. As a consequence, the performance of the NTPV system is significantly improved. The energy efficiency can reach nearly 53% of  $\eta_C$  while the heat source and the photovoltaic cell are kept at a relatively low temperature difference (130 K). The underlying mechanism is uncovered as the topological transitions in the near-field coupled photonic systems, specifically, in the forms of SPhPs. Meanwhile, the output power can also be tuned by twisting the  $h$ -BN metasurface. Our study paves the pathway toward high-performance TPV systems based on twisted photonics. Another possible application for this two-dimensional twisted material system could be photodetectors, which may be considered in the future.

#### ACKNOWLEDGMENTS

We are grateful for support through funding for Distinguished Young Scientist from the National Natural Science Foundation of China (Grants No. 12125504, No. 12074281, No. 12074281, No. 12047541, No. 12074279, and No. 52106099), the Major Program of Natural Science Research of Jiangsu Higher Education Institutions (Grant No. 18KJA140003), the Jiangsu Specially Appointed Professor funding, and the Academic Program Development of Jiangsu Higher Education (PAPD), the China Postdoctoral Science Foundation (Grant No. 2020M681376),

the faculty start-up funding of Suzhou University of Science and Technology, and Jiangsu Key Disciplines of the Fourteenth Five-Year Plan (Grant No. 2021135).

#### APPENDIX A: CALCULATION OF THE REFLECTION AND TRANSMISSION COEFFICIENTS

To calculate the photon transmission coefficient between the near-field emitter and the cell, it is necessary to calculate the reflection and transmission coefficients at different values of the azimuth angle  $\phi$  [48]. When  $\phi$  is not equal to 0, the plane of incidence is tilted off the  $x$  axis by an angle  $\phi$ . Following the procedure of Ref. [48], we calculate the reflection and transmission coefficients in the  $x'y'z'$  coordinate system. The permittivity tensor in the  $x'y'z'$  coordinate system can be expressed as

$$\begin{pmatrix} \varepsilon_{xx} & \varepsilon_{xy} & \varepsilon_{xz} \\ \varepsilon_{yx} & \varepsilon_{yy} & \varepsilon_{yz} \\ \varepsilon_{zx} & \varepsilon_{zy} & \varepsilon_{zz} \end{pmatrix} = \mathbf{T}_z \boldsymbol{\varepsilon} \mathbf{T}_z^{-1}, \quad (\text{A1})$$

where  $\mathbf{T}_z$  is the coordinate rotational transformation matrix and  $\boldsymbol{\varepsilon}$  is the permittivity tensor of any anisotropic material in the  $xyz$  coordinate system. The matrix  $\mathbf{T}_z$  is given as

$$\mathbf{T}_z = \begin{pmatrix} \cos \phi & \sin \phi & 0 \\ -\sin \phi & \cos \phi & 0 \\ 0 & 0 & 1 \end{pmatrix}. \quad (\text{A2})$$

If the incident wave is a transverse electric wave, the electromagnetic fields in the medium can be written with reference to the  $x'y'z'$  coordinate system as

$$\mathbf{E} = \mathbf{S}(z) \exp(-i\omega t + i\beta x) \quad (\text{A3})$$

and

$$\mathbf{H} = -i\sqrt{\varepsilon_0/\mu_0} \mathbf{U}(z) \exp(-i\omega t + i\beta x), \quad (\text{A4})$$

where  $\mathbf{S} = (S_x, S_y, S_z)$  and  $\mathbf{H} = (U_x, U_y, U_z)$ .

In the above equations, the prime on the space variables has been dropped for brevity and  $\beta$  is the wave-vector component along the  $x$  axis. The wave-vector component along the  $z$  axis in vacuum is  $k_z = \sqrt{k_0^2 - \beta^2}$ . Substituting Eqs. (A1), (A3), and (A4) into the Maxwell equations and setting  $K_x = \beta/k_0$ , we obtain the differential equations

$$\frac{d}{dz} \begin{pmatrix} S_x \\ S_y \\ U_x \\ U_y \end{pmatrix} = k_0 \mathbf{M} \begin{pmatrix} S_x \\ S_y \\ U_x \\ U_y \end{pmatrix}, \quad (\text{A5})$$

where the coefficients matrix is given by

$$\mathbf{M} = \begin{pmatrix} -iK_x\epsilon_{zx}/\epsilon_{zz} & -iK_x\epsilon_{zy}/\epsilon_{zz} & 0 & K_x^2/\epsilon_{zz} - 1 \\ 0 & 0 & 1 & 0 \\ \epsilon_{yz}\epsilon_{zx}/\epsilon_{zz} - \epsilon_{yx} & \epsilon_{yz}\epsilon_{zy}/\epsilon_{zz} + K_x^2 - \epsilon_{yy} & 0 & iK_x\epsilon_{yz}/\epsilon_{zz} \\ \epsilon_{xx} - \epsilon_{xz}\epsilon_{zx}/\epsilon_{zz} & \epsilon_{xy} - \epsilon_{xz}\epsilon_{zy}/\epsilon_{zz} & 0 & -iK_x\epsilon_{xz}/\epsilon_{zz} \end{pmatrix}. \quad (\text{A6})$$

Assuming  $U = (S_x S_y U_x U_y)^T$ , we have  $\mathbf{M}U = qU$ . By solving the equation, i.e.,  $|\mathbf{M} - q\mathbf{I}| = 0$ , we obtain four eigenvalues  $q_m$ ,  $m = 1, 2, 3, 4$ , of the matrix  $\mathbf{M}$  and corresponding eigenvectors

$$\omega_m = \begin{pmatrix} w_{1,m} \\ w_{2,m} \\ w_{3,m} \\ w_{4,m} \end{pmatrix}, \quad m = 1, 2, 3, 4. \quad (\text{A7})$$

For the near-field emitter consisting of *h*-BN grating with thickness  $t_{\text{BN}}$ , the electromagnetic fields in the medium can be described by the eigenvalues and eigenvectors of the coefficient matrix

$$S_x(z) = \sum_{m=1}^2 w_{1,m} c_m^+ \exp(k_0 q_m z) + \sum_{m=1}^2 w_{1,m+2} c_m^- \exp[-k_0 q_m (z - t_{\text{BN}})], \quad (\text{A8})$$

$$S_y(z) = \sum_{m=1}^2 w_{2,m} c_m^+ \exp(k_0 q_m z) + \sum_{m=1}^2 w_{2,m+2} c_m^- \exp[-k_0 q_m (z - t_{\text{BN}})], \quad (\text{A9})$$

$$U_x(z) = \sum_{m=1}^2 w_{3,m} c_m^+ \exp(k_0 q_m z) + \sum_{m=1}^2 w_{3,m+2} c_m^- \exp[-k_0 q_m (z - t_{\text{BN}})], \quad (\text{A10})$$

$$U_y(z) = \sum_{m=1}^2 w_{4,m} c_m^+ \exp(k_0 q_m z) + \sum_{m=1}^2 w_{4,m+2} c_m^- \exp[-k_0 q_m (z - t_{\text{BN}})], \quad (\text{A11})$$

In the above equations, the real parts of the eigenvalues  $q_m$ ,  $m = 1, 2, 3, 4$ , are positive; and  $c_m^+$  and  $c_m^-$  are unknowns which can be determined by matching the boundary conditions. The reflection and transmission coefficients can be calculated by applying the tangential electric and magnetic field components at the top and the bottom surfaces of the

grating, respectively,

$$\begin{pmatrix} 0 \\ 1 \\ ik_z/k_0 \\ 0 \end{pmatrix} \begin{pmatrix} -k_z/k_0 & 0 \\ 0 & 1 \\ 0 & -ik_z/k_0 \\ -i & 0 \end{pmatrix} \begin{pmatrix} r_{sp} \\ r_{ss} \end{pmatrix} = (\mathbf{W}_1 \quad \mathbf{W}_2 \mathbf{X}) \begin{pmatrix} \mathbf{C}^+ \\ \mathbf{C}^- \end{pmatrix} \quad (\text{A12})$$

and

$$(\mathbf{W}_1 \mathbf{Y} \quad \mathbf{W}_2) \begin{pmatrix} \mathbf{C}^+ \\ \mathbf{C}^- \end{pmatrix} = \begin{pmatrix} k_z/k_0 & 0 \\ 0 & 1 \\ 0 & ik_z/k_0 \\ -i & 0 \end{pmatrix} \begin{pmatrix} t_{sp} \\ t_{ss} \end{pmatrix}. \quad (\text{A13})$$

Here  $\mathbf{W} = (\mathbf{W}_1 \quad \mathbf{W}_2)$  is the eigenvector of the matrix  $\mathbf{M}$ ;  $\mathbf{C}^+$  and  $\mathbf{C}^-$  are vectors composed of the unknowns;  $\mathbf{X}$  is a diagonal matrix with diagonal elements  $\exp(-k_0 q_m t_{\text{BN}})$ ,  $m = 3, 4$ ; and  $\mathbf{Y}$  is a diagonal matrix with diagonal elements  $\exp(k_0 q_m t_{\text{BN}})$ ,  $m = 1, 2$ .

Likewise, when the incident wave is a transverse magnetic wave, the electromagnetic fields in the medium can be written as

$$\mathbf{H} = \mathbf{U}(z) \exp(-i\omega t + i\beta x) \quad (\text{A14})$$

and

$$\mathbf{E} = i\sqrt{\mu_0/\epsilon_0} \mathbf{S}(z) \exp(-i\omega t + i\beta x). \quad (\text{A15})$$

By substituting Eqs. (A14) and (A15) into the Maxwell equations, the same differential equations as those in Eq. (A5) can be obtained with exactly the same coefficient matrix as shown in Eq. (A). One can express the fields in the uniaxial medium in the same forms as in Eqs. (A8)–(A11) and apply the boundary conditions at the top and bottom surfaces of the grating, which are, respectively, expressed as

$$\begin{pmatrix} ik_z/k_0 \\ 0 \\ 0 \\ 1 \end{pmatrix} \begin{pmatrix} -ik_z/k_0 & 0 \\ 0 & i \\ 0 & k_z/k_0 \\ 1 & 0 \end{pmatrix} \begin{pmatrix} r_{pp} \\ r_{ps} \end{pmatrix} = (\mathbf{W}_1 \quad \mathbf{W}_2 \mathbf{X}) \begin{pmatrix} \mathbf{C}^+ \\ \mathbf{C}^- \end{pmatrix} \quad (\text{A16})$$

and

$$(\mathbf{W}_1 \mathbf{Y} - \mathbf{W}_2) \begin{pmatrix} \mathbf{C}^+ \\ \mathbf{C}^- \end{pmatrix} = \begin{pmatrix} ik_z/k_0 & 0 \\ 0 & i \\ 0 & -k_z/k_0 \\ 1 & 0 \end{pmatrix} \begin{pmatrix} t_{pp} \\ t_{ps} \end{pmatrix}. \quad (\text{A17})$$

Next, we extend the above analysis to an arbitrary  $L$ -layer structure by matching the tangential electric and magnetic field components at each interface. Take the incidence of a transverse magnetic wave for an example. All the boundary conditions are

$$\begin{pmatrix} ik_z/k_0 \\ 0 \\ 0 \\ 1 \end{pmatrix} + \begin{pmatrix} -ik_z/k_0 & 0 \\ 0 & i \\ 0 & k_z/k_0 \\ 1 & 0 \end{pmatrix} \begin{pmatrix} r_{pp} \\ r_{ps} \end{pmatrix} = (\mathbf{W}_{(1)1} - \mathbf{W}_{(1)2} \mathbf{X}_{(1)}) \begin{pmatrix} \mathbf{C}_{(1)}^+ \\ \mathbf{C}_{(1)}^- \end{pmatrix}, \quad (\text{A18})$$

$$\begin{aligned} & (\mathbf{W}_{(l-1)1} \mathbf{Y}_{(l-1)} - \mathbf{W}_{(l-1)2}) \begin{pmatrix} \mathbf{C}_{(l-1)}^+ \\ \mathbf{C}_{(l-1)}^- \end{pmatrix} \\ &= (\mathbf{W}_{(l)1} \mathbf{Y}_{(l)} - \mathbf{W}_{(l)2}) \begin{pmatrix} \mathbf{C}_{(l)}^+ \\ \mathbf{C}_{(l)}^- \end{pmatrix}, \end{aligned} \quad (\text{A19})$$

and

$$\begin{aligned} & (\mathbf{W}_{(L)1} \mathbf{Y}_{(L)} - \mathbf{W}_{(L)2}) \begin{pmatrix} \mathbf{C}_{(L)}^+ \\ \mathbf{C}_{(L)}^- \end{pmatrix} \\ &= \begin{pmatrix} ik_z/k_0 & 0 \\ 0 & i \\ 0 & -k_z/k_0 \\ 1 & 0 \end{pmatrix} \begin{pmatrix} t_{pp} \\ t_{ps} \end{pmatrix}, \end{aligned} \quad (\text{A20})$$

where  $l = 2, 3, \dots, L$ . Above,  $\mathbf{W}_{(l)}$ ,  $\mathbf{X}_{(l)}$ , and  $\mathbf{Y}_{(l)}$  have the same definitions as  $\mathbf{W}$ ,  $\mathbf{X}$ , and  $\mathbf{Y}$  described previously. For each  $l$ ,  $\mathbf{W}_{(l)} = (\mathbf{W}_{(l)1} \mathbf{W}_{(l)2})$ .

To avoid the numerical instability associated with the inversion of the matrix, we adopt the enhanced transmittance matrix approach. From Eq. (A30), one has

$$\begin{pmatrix} \mathbf{C}_{(L)}^+ \\ \mathbf{C}_{(L)}^- \end{pmatrix} = (\mathbf{W}_{(L)1} \mathbf{Y}_{(L)} \mathbf{W}_{(L)2})^{-1} \begin{pmatrix} \mathbf{f}_{(L+1)} \\ \mathbf{g}_{(L+1)} \end{pmatrix} \mathbf{t}, \quad (\text{A21})$$

where

$$\begin{aligned} \mathbf{t} &= \begin{pmatrix} t_{pp} \\ t_{ps} \end{pmatrix}, \quad \mathbf{f}_{(L+1)} \begin{pmatrix} ik_z/k_0 & 0 \\ 0 & i \end{pmatrix}, \\ \mathbf{g}_{(L+1)} &= \begin{pmatrix} 0 & -k_z/k_0 \\ 1 & 0 \end{pmatrix}. \end{aligned} \quad (\text{A22})$$

To ensure that the matrix to be inverted in Eq. (A21) is numerically stable, we follow the procedure given by

Moharam *et al.* [62], and rewrite it as the product of two matrices:

$$(\mathbf{W}_{(L)1} \mathbf{Y}_{(L)} \mathbf{W}_{(L)2})^{-1} = \begin{pmatrix} \mathbf{Y}_{(L)} & 0 \\ 0 & \mathbf{I} \end{pmatrix}^{-1} (\mathbf{W}_{(L)1} \mathbf{W}_{(L)2})^{-1}. \quad (\text{A23})$$

The matrix on the right in the product is well conditioned, and its inversion is numerically stable. Therefore, Eq. (A21) can be rearranged as

$$\begin{pmatrix} \mathbf{C}_{(L)}^+ \\ \mathbf{C}_{(L)}^- \end{pmatrix} = (\mathbf{W}_{(L)1} \mathbf{Y}_{(L)} \mathbf{W}_{(L)2})^{-1} \begin{pmatrix} \mathbf{a}_L \\ \mathbf{b}_L \end{pmatrix} \mathbf{t}, \quad (\text{A24})$$

where  $\mathbf{I}$  is the unit matrix and

$$\begin{pmatrix} \mathbf{a}_L \\ \mathbf{b}_L \end{pmatrix} = (\mathbf{W}_{(L)1} \mathbf{W}_{(L)2})^{-1} \begin{pmatrix} \mathbf{f}_{(L+1)} \\ \mathbf{g}_{(L+1)} \end{pmatrix}. \quad (\text{A25})$$

We adopt the substitution  $\mathbf{t} = \mathbf{a}_L^{-1} \mathbf{Y}_L \mathbf{t}_L$ , and then Eq. (A24) becomes

$$\begin{pmatrix} \mathbf{C}_{(L)}^+ \\ \mathbf{C}_{(L)}^- \end{pmatrix} = \begin{pmatrix} \mathbf{b}_L \mathbf{a}_L^{-1} \mathbf{Y}_{(L)} & \mathbf{I} \end{pmatrix} \mathbf{t}_L. \quad (\text{A26})$$

Putting Eq. (A26) into Eq. (A19) for  $l = L$ , we have

$$\begin{pmatrix} \mathbf{C}_{(L-1)}^+ \\ \mathbf{C}_{(L-1)}^- \end{pmatrix} = (\mathbf{W}_{(L-1)1} \mathbf{Y}_{(L-1)} \mathbf{W}_{(L-1)2})^{-1} \begin{pmatrix} \mathbf{f}_L \\ \mathbf{g}_L \end{pmatrix} \mathbf{t}_L, \quad (\text{A27})$$

where

$$\begin{pmatrix} \mathbf{f}_L \\ \mathbf{g}_L \end{pmatrix} = \mathbf{W}_{(L)1} + \mathbf{W}_{(L)2} \mathbf{X}_{(L)} \mathbf{b}_L \mathbf{a}_L^{-1} \mathbf{L}_{(L)}. \quad (\text{A28})$$

Repeating the above procedure for all layers, we obtain

$$\begin{aligned} & \begin{pmatrix} ik_z/k_0 \\ 0 \\ 0 \\ 1 \end{pmatrix} + \begin{pmatrix} -ik_z/k_0 & 0 \\ 0 & i \\ 0 & k_z/k_0 \\ 1 & 0 \end{pmatrix} \mathbf{r} = \begin{pmatrix} \mathbf{f}_1 \\ \mathbf{g}_1 \end{pmatrix} \mathbf{t}_1, \\ & \mathbf{r} = \begin{pmatrix} r_{pp} \\ r_{ps} \end{pmatrix}. \end{aligned} \quad (\text{A29})$$

We can solve Eq. (A29) for  $r_{pp}$ ,  $r_{ps}$ , and  $\mathbf{t}_1$ , and then the transmission coefficients can be calculated as

$$\begin{pmatrix} t_{pp} \\ t_{ps} \end{pmatrix} = \mathbf{a}_L^{-1} \mathbf{Y}_{(L)} \mathbf{a}_{L-1}^{-1} \mathbf{Y}_{(L-1)} \cdots \mathbf{a}_1^{-1} \mathbf{Y}_1^{-1} \mathbf{t}_1. \quad (\text{A30})$$

The procedure is basically the same as above for the incidence of a transverse electrical wave.

## APPENDIX B: EFFECTS OF OUT-OF-PLANE AND IN-PLANE TWISTS ON THE PHOTON TRANSMISSIONS OF NTPV SYSTEMS

To better understand the underlying mechanism of the contributions of the three modes (modes ①, ②, and ③), we present the energy transmission coefficients  $\zeta$  in the  $k_x$ - $k_y$  plane, as shown in Fig. 4. In the system with  $A = h\text{-BN}$  thin film (with the optical axis in the  $z$  direction), the photon transmission is enhanced in the two hyperbolic regions

of  $h\text{-BN}$ . The enhanced transmission below the gap frequency of the InSb  $p$ - $n$  junction (mode ①, about  $1.55 \times 10^{14}$  rad/s) is due to the strong coupling of the ESPHPs supported by the  $h\text{-BN}$  thin films of the emitter and the cell. The high transmission above the gap frequency of the InSb  $p$ - $n$  junction (mode ②, about  $2.62 \times 10^{14}$  rad/s, and mode ③, about  $2.81 \times 10^{14}$  rad/s) originates from the resonant coupling between the ESPHPs in  $h\text{-BN}$  and the electron-hole excitations in the InSb  $p$ - $n$  junction. As

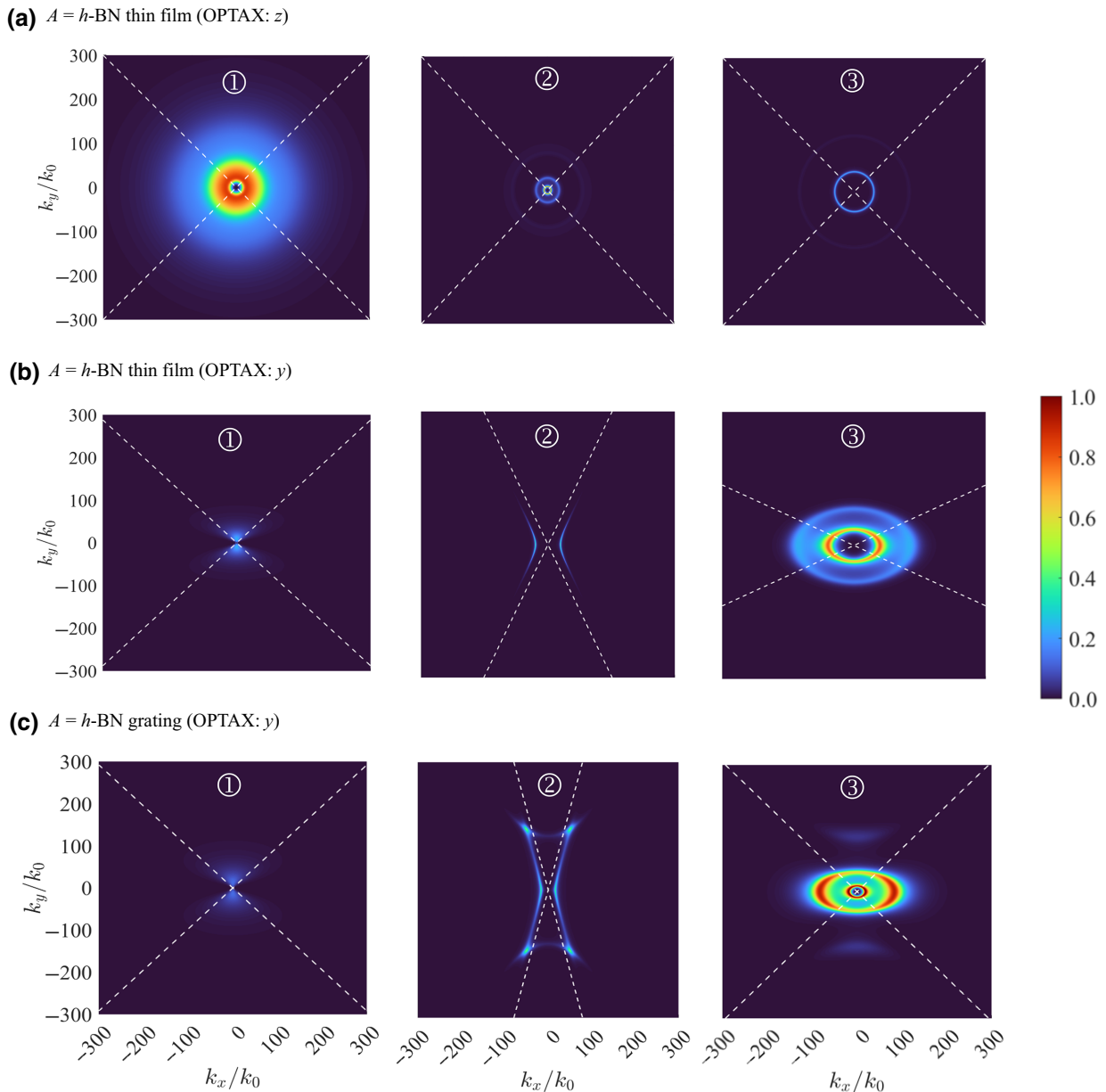


FIG. 4. The photon transmission coefficients of the  $A$ - $A$ -InSb NTPV systems with (a)  $A = h\text{-BN}$  thin film (with the optical axis in the  $z$  direction), (b)  $A = h\text{-BN}$  thin film (with the optical axis in the  $y$  direction), and (c)  $A = h\text{-BN}$  grating (with the optical axis in the  $y$  direction). Parameters: the thickness of both the  $h\text{-BN}$  thin film and the metasurface is  $h_{\text{BN}} = 10$  nm; the periodicity and the filling factor of the  $h\text{-BN}$  metasurface are  $p = 100$  nm and  $\xi = 0.4$ , respectively. The temperature of the emitter and the cell are set at  $T_{\text{emit}} = 450$  K and  $T_{\text{cell}} = 320$  K, respectively. The vacuum gap distance is  $d = 20$  nm.

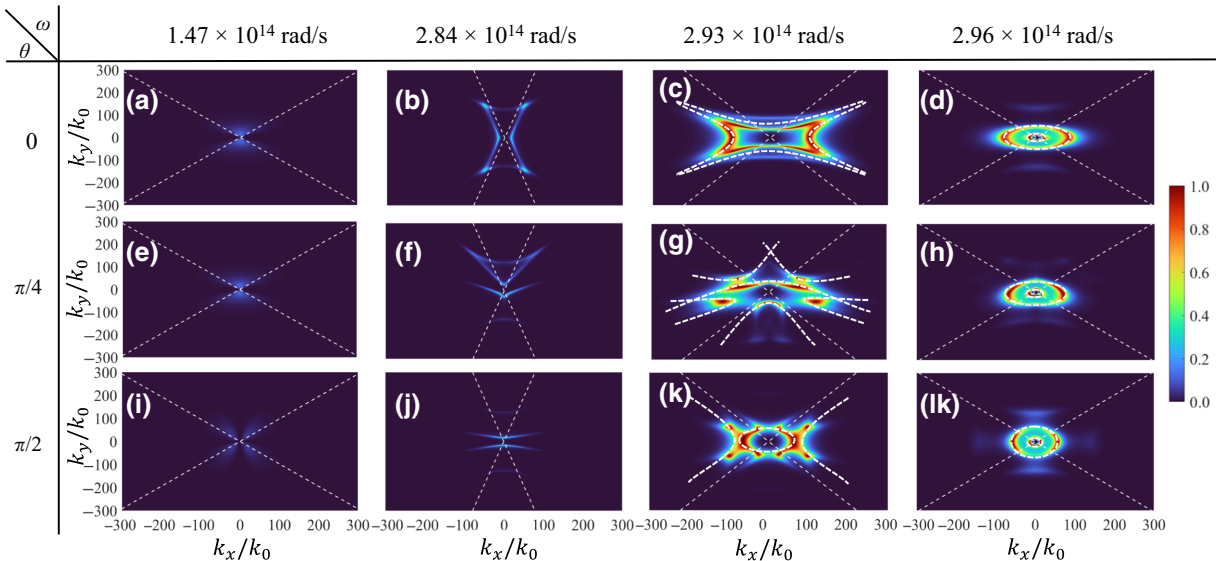


FIG. 5. Anisotropic energy transmission coefficients of the NTPV system based on *h*-BN gratings for different twisting angles at different frequencies. The thickness of the *h*-BN metasurface is set as  $h_{\text{BN}} = 10$  nm. The periodicity and the filling factor of the *h*-BN metasurface are  $p = 100$  nm and  $\xi = 0.4$ , respectively. The temperature of the emitter and the cell are set at  $T_{\text{emit}} = 450$  K and  $T_{\text{cell}} = 320$  K, respectively. The vacuum gap distance is  $d = 20$  nm.

confirmed by the energy transmission coefficients varying with the wave-vector components  $k_x$  and  $k_y$ , shown in Fig. 4(a), the high energy transmission coefficient exhibits rotational symmetry in the  $k_x$ - $k_y$  plane for all three modes, which is due to the in-plane isotropic nature of *h*-BN. It is also noted that the photon transmission around mode ① is much stronger than the other two modes, the bright circular region centered at the region and with radius far exceeding  $k_0$ , which indicates the strong coupling of ESPHPs between the *h*-BN thin films.

After twisting the optical axis to the  $y$  direction, the below-gap transmission (mode ①, about  $1.55 \times 10^{14}$  rad/s) and one above-gap transmission (mode ②, about  $2.73 \times 10^{14}$  rad/s) are both weakened, with reduced transmission probability and wave-vector range  $k_{\max} < 100k_0$ , as shown in Fig. 2(b). This is due to the topological transition induced by the twist of the optical axis. At mode ① (about  $1.55 \times 10^{14}$  rad/s) and mode ② (about  $2.73 \times 10^{14}$  rad/s), the HSPHPs are excited and dominate the energy transfer due to the in-plane anisotropy. Specifically, the permittivities are  $\varepsilon_{\perp} = 7.7707 - 0.0099i$  and  $\varepsilon_{\parallel} = -0.5455 - 0.1696j$  at mode ① (about  $1.55 \times 10^{14}$  rad/s) and  $\varepsilon_{\perp} = -10.8946 + 0.5172i$  and  $\varepsilon_{\parallel} = 2.7905 + 0.0006i$  at mode ②, respectively. Because of the opposite signs of the permittivities, the dispersion of HSPHPs is satisfied, which gives rise to the hyperbolic transmission contour [48]. In addition, there appears another enhanced transmission (mode ③, about  $2.99 \times 10^{14}$  rad/s) in the type II hyperbolic band of *h*-BN. For this mode, the permittivities are  $\varepsilon_{\perp} = -0.5775 + 0.0675i$  and  $\varepsilon_{\parallel} = 2.8255 + 0.0004i$ , which satisfy the dispersion of the ESPHPs. Because of

the strong coupling of the ESPHPs between the emitter and the cell, the photon transmission around this mode is much enhanced compared to the case in Fig. 4(a), with increased transmission probability and wave-vector range  $k_{\max} \approx 180k_0$ .

From Fig. 2(c), we find that, when the *h*-BN thin film is patterned into a metasurface structure (with  $p = 100$  nm,  $\xi = 0.4$ ), the above-gap transmission modes ② (about  $2.83 \times 10^{14}$  rad/s) and ③ (about  $2.96 \times 10^{14}$  rad/s) of the NTPV system are further enhanced and merge into one strong resonant mode. As shown in Fig. 4(c), the transmission contour is similar to that of the system with  $A = \text{h-BN}$  thin film (with the optical axis in the  $y$  direction) at mode ① (about  $1.55 \times 10^{14}$  rad/s). For mode ② (about  $2.83 \times 10^{14}$  rad/s), the in-plane hyperbolic dispersion ( $\varepsilon_x = -47.9263 + 14.5097i$ ,  $\varepsilon_y = 0.0003 + 0.1102i$ ) is formed by near-field coupling of the phonon polaritons in individual *h*-BN nanoribbons [43]. Because of the contribution of these HSPHPs, the enhanced transmission contour at this mode exhibits strong hyperbolicity, and more HSPHPs are excited and contribute to the energy transfer. For ③ (about  $2.96 \times 10^{14}$  rad/s), the phonon polaritons have elliptical in-plane dispersion with  $\varepsilon_x = -2.1815 + 0.2079i$ ,  $\varepsilon_y = -2.0932 + 0.0002i$ . Originating from the strong collective near-field coupling of individual nanoresonators, the ESPHPs are excited and contribute to the elliptical contour of the enhanced transmission.

To demonstrate the optimization nature of the TPV energy efficiency with twist-induced topological transition, we drew several plots of transmission with different in-plane twist angles, as indicated in Fig. 5. To

characterize the topological nature of SPhPs, we show transmission in  $k_x$ - $k_y$  space with four resonant frequencies at different in-plane twist angles. The four resonant frequencies are around mode ① (about  $1.47 \times 10^{14}$  rad/s), mode ② (about  $2.83 \times 10^{14}$  rad/s), mode ③ (about  $2.96 \times 10^{14}$  rad/s), and a resonant mode (about  $2.93 \times 10^{14}$  rad/s) between mode ② and mode ③. For the system with zero in-plane twist, the HSPhPs around mode ② and the ESPhPs around mode ③ are coupled and form a strong resonant mode at  $2.93 \times 10^{14}$  rad/s. With the twist angle changing from zero to  $\pi/2$ , the bright band of the photon transmission at this resonant frequency changes from hyperbolic (open) to elliptical (closed). In the meantime, there is band splitting when the twist angle changes from zero to  $\pi/4$  and there is band degeneracy when the twist angle changes from  $\pi/4$  to  $\pi/2$ . It is also noticed that the contribution of HSPhPs with larger wave-vectors are suppressed and the ESPhPs with lower wave-vectors dominate the photon tunneling, which leads to the weakened photon transmission above the gap frequency in Figs. 2(d) and 2(e).

- 
- [1] T. Bauer, *Thermophotovoltaics: Basic Principles and Critical Aspects of System Design* (Springer Science & Business Media, Berlin, Germany, 2011).
- [2] W. R. Chan, P. Bermel, R. C. N. Pilawa-Podgurski, C. H. Marton, K. F. Jensen, J. J. Senkevich, J. D. Joannopoulos, M. Soljačić, and I. Celanovic, Toward high-energy-density, high-efficiency, and moderate-temperature chip-scale thermophotovoltaics, *Proc. Natl. Acad. Sci.* **110**, 5309 (2013).
- [3] A. LaPotin, K. L. Schulte, M. A. Steiner, K. Buznitsky, C. C. Kelsall, D. J. Friedman, E. J. Tervo, R. M. France, M. R. Young, A. Rohskopf, S. Verma, E. N. Wang, and A. Henry, Thermophotovoltaic efficiency of 40, *Nature* **604**, 287 (2022).
- [4] T. Liao, L. Cai, Y. Zhao, and J. Chen, Efficiently exploiting the waste heat in solid oxide fuel cell by means of thermophotovoltaic cell, *J. Power Sources* **306**, 666 (2016).
- [5] E. Tervo, E. Bagherisereshki, and Z. M. Zhang, Near-field radiative thermoelectric energy converters: A review, *Front. Energy* **12**, 5 (2018).
- [6] S.-A. Biehs, R. Messina, P. S. Venkataram, A. W. Rodriguez, J. C. Cuevas, and P. Ben-Abdallah, Near-field radiative heat transfer in many-body systems, *Rev. Mod. Phys.* **93**, 025009 (2021).
- [7] S. Molesky and Z. Jacob, Ideal near-field thermophotovoltaic cells, *Phys. Rev. B* **91**, 205435 (2015).
- [8] Raphael St-Gelais, Gaurang Ravindra Bhatt, Linxiao Zhu, Shanhui Fan, and Michal Lipson, Hot carrier-based near-field thermophotovoltaic energy conversion, *ACS Nano* **11**, 3001 (2017).
- [9] Georgia T. Papadakis, Siddharth Buddhiraju, Zhixin Zhao, Bo Zhao, and Shanhui Fan, Broadening near-field emission for performance enhancement in thermophotovoltaics, *Nano Lett.* **20**, 1654 (2020).
- [10] Bo Zhao, Kaifeng Chen, Siddharth Buddhiraju, Gaurang Bhatt, Michal Lipson, and Shanhui Fan, High-performance near-field thermophotovoltaics for waste heat recovery, *Nano Energy* **41**, 344 (2017).
- [11] Bo Zhao, Parthiban Santhanam, Kaifeng Chen, Siddharth Buddhiraju, and Shanhui Fan, Near-field thermophotonic systems for low-grade waste-heat recovery, *Nano Lett.* **18**, 5224 (2018).
- [12] R. S. DiMatteo, P. Greiff, S. L. Finberg, K. A. Young-Waithe, H. K. H. Choy, M. M. Masaki, and C. G. Fonstad, Enhanced photogeneration of carriers in a semiconductor via coupling across a nonisothermal nanoscale vacuum gap, *Appl. Phys. Lett.* **79**, 1894 (2001).
- [13] K. Kim, B. Song, V. Fernández-Hurtado, W. Lee, W. Jeong, L. Cui, D. Thompson, J. Feist, M. T. H. Reid, F. J. García-Vidal, J. C. Cuevas, E. Meyhofer, and P. Reddy, Radiative heat transfer in the extreme near field, *Nature* **528**, 387 (2015).
- [14] A. Fiorino, D. Thompson, L. Zhu, B. Song, P. Reddy, and E. Meyhofer, Giant enhancement in radiative heat transfer in sub-30 nm gaps of plane parallel surfaces, *Nano Lett.* **18**, 3711 (2018).
- [15] A. Fiorino, L. Zhu, D. Thompson, R. Mittapally, P. Reddy, and E. Meyhofer, Nanogap near-field thermophotovoltaics, *Nat. Nanotechnol.* **13**, 806 (2018).
- [16] J. Desutter, L. Tang, and M. Francoeur, A near-field radiative heat transfer device, *Nat. Nanotechnol.* **14**, 751 (2019).
- [17] T. Inoue, T. Koyama, D. D. Kang, K. Ikeda, T. Asano, and S. Noda, One-chip near-field thermophotovoltaic device integrating a thin-film thermal emitter and photovoltaic cell, *Nano Lett.* **19**, 3948 (2019).
- [18] C. Lucchesi, D. Cakiroglu, J.-P. Perez, T. Taliercio, E. Tournié, P.-O. Chapuis, and R. Vaillon, Near-field thermophotovoltaic conversion with high electrical power density and cell efficiency above 14, *Nano Lett.* **21**, 4524 (2021).
- [19] R. Mittapally, B. Lee, L. Zhu, A. Reihani, J. W. Lim, D. Fan, S. R. Forrest, P. Reddy, and E. Meyhofer, Near-field thermophotovoltaics for efficient heat to electricity conversion at high power density, *Nat. Commun.* **12**, 4364 (2021).
- [20] J. Song, J. Jang, M. Lim, M. Choi, J. Lee, and B. J. Lee, Thermophotovoltaic energy conversion in far-to-near-field transition regime, *ACS Photonics* **9**, 1748 (2022).
- [21] Lei Tang, John DeSutter, and Mathieu Francoeur, Near-field radiative heat transfer between dissimilar materials mediated by coupled surface phonon- and plasmon-polaritons, *ACS Photonics* **7**, 1304 (2020).
- [22] Yong Zhang, Cheng-Long Zhou, Lei Qu, and Hong-Liang Yi, Active control of near-field radiative heat transfer through nonreciprocal graphene surface plasmons, *Appl. Phys. Lett.* **116**, 151101 (2020).
- [23] S.-A. Biehs, Maria Tschikin, and Philippe Ben-Abdallah, Hyperbolic Metamaterials as an Analog of a Blackbody in the Near Field, *Phys. Rev. Lett.* **109**, 104301 (2012).
- [24] Mohammad Ghashami, Hongyao Geng, Taehoon Kim, Nicholas Iacopino, Sung Kwon Cho, and Keunhan Park, Precision Measurement of Phonon-Polaritonic Near-Field Energy Transfer Between Macroscale Planar Structures Under Large Thermal Gradients, *Phys. Rev. Lett.* **120**, 175901 (2018).

- [25] Huihai Wu, Yong Huang, Longji Cui, and Keyong Zhu, Active Magneto-Optical Control of Near-Field Radiative Heat Transfer Between Graphene Sheets, *Phys. Rev. Appl.* **11**, 054020 (2019).
- [26] J. Peng, G. Tang, L. Wang, R. Macêdo, H. Chen, and J. Ren, Twist-induced near-field thermal switch using non-reciprocal surface magnon-polaritons, *ACS Photonics* **8**, 2183 (2021).
- [27] C. Wu, B. Neuner III, J. John, A. Milder, B. Zollars, S. Savoy, and G. Shvets, Metamaterial-based integrated plasmonic absorber/emitter for solar thermo-photovoltaic systems, *J. Optics* **14**, 024005 (2012).
- [28] V. B. Svetovoy, P. J. Van Zwol, and J. Chevrier, Plasmon enhanced near-field radiative heat transfer for graphene covered dielectrics, *Phys. Rev. B* **85**, 155418 (2012).
- [29] O. Ilic, M. Jablan, J. D. Joannopoulos, I. Celanovic, and M. Soljačić, Overcoming the black body limit in plasmonic and graphene near-field thermophotovoltaic systems, *Opt. Express* **20**, A366 (2012).
- [30] V. B. Svetovoy and G. Palasantzas, Graphene-on-Silicon Near-Field Thermophotovoltaic Cell, *Phys. Rev. Appl.* **2**, 034006 (2014).
- [31] Soumyadipta Basu, Yue Yang, and Liping Wang, Near-field radiative heat transfer between metamaterials coated with silicon carbide thin films, *Appl. Phys. Lett.* **106**, 033106 (2015).
- [32] G. R. Bhatt, B. Zhao, S. Roberts, I. Datta, A. Mohanty, T. Lin, J.-M. Hartmann, R. St-Gelais, S. Fan, and M. Lipson, Integrated near-field thermo-photovoltaics for heat recycling, *Nat. Commun.* **11**, 1 (2020).
- [33] R. Mittapally, B. Lee, L. Zhu, A. Reihani, J. W. Lim, D. Fan, S. R. Forrest, P. Reddy, and E. Meyhofer, Near-field thermophotovoltaics for efficient heat to electricity conversion at high power density, *Nat. Commun.* **12**, 1 (2021).
- [34] B. Zhao, B. Guizal, Z. M. Zhang, S. Fan, and M. Antezza, Near-field heat transfer between graphene/hBN multilayers, *Phys. Rev. B* **95**, 245437 (2017).
- [35] R. Liu, C. Zhou, Y. Zhang, Z. Cui, X. Wu, and H. Yi, Near-field radiative heat transfer in hyperbolic materials, *Int. J. Extreme Manuf.* **4**, 032002 (2022).
- [36] L. Lu, B. Zhang, H. Ou, B. Li, K. Zhou, J. Song, Z. Luo, and Q. Cheng, Enhanced near-field radiative heat transfer between graphene/hBN systems, *Small* **18**, 2108032 (2022).
- [37] Guangwei Hu, Alex Krasnok, Yarden Mazor, Cheng-Wei Qiu, and Andrea Alù, Moiré hyperbolic metasurfaces, *Nano Lett.* **20**, 3217 (2020).
- [38] Guangwei Hu, Qingdong Ou, Guangyuan Si, Yingjie Wu, Jing Wu, Zhigao Dai, Alex Krasnok, Yarden Mazor, Qing Zhang, and Qiaoliang Bao, *et al.*, Topological polaritons and photonic magic angles in twisted  $\alpha$ -MoO<sub>3</sub> bilayers, *Nature* **582**, 209 (2020).
- [39] Mingjian He, Hong Qi, Yatao Ren, Yijun Zhao, and Mauro Antezza, Active control of near-field radiative heat transfer by a graphene-gratings coating-twisting method, *Opt. Lett.* **45**, 2914 (2020).
- [40] Cheng-Long Zhou, Xiao-Hu Wu, Yong Zhang, Hong-Liang Yi, and Mauro Antezza, Polariton topological transition effects on radiative heat transfer, *Phy. Rev. B* **103**, 155404 (2021).
- [41] J. Sebastian Gomez-Diaz, Mykhailo Tymchenko, and Andrea Alù, Hyperbolic Plasmons and Topological Transitions Over Uniaxial Metasurfaces, *Phys. Rev. Lett.* **114**, 233901 (2015).
- [42] J. S. Gomez-Diaz and Andrea Alu, Flatland optics with hyperbolic metasurfaces, *ACS Photonics* **3**, 2211 (2016).
- [43] P. Li, G. Hu, I. Dolado, M. Tymchenko, C.-W. Qiu, F. J. Alfaro-Mozaz, F. Casanova, L. E. Hueso, S. Liu, J. H. Edgar, S. Velez, A. Alu, and R. Hillenbrand, Collective near-field coupling and nonlocal phenomena in infrared-phononic metasurfaces for nano-light canalization, *Nat. Commun.* **11**, 1 (2020).
- [44] R. Wang, J. Lu, and J.-H. Jiang, Enhancing Thermophotovoltaic Performance Using Graphene-BN-InSb Near-Field Heterostructures, *Phys. Rev. Appl.* **12**, 044038 (2019).
- [45] R. Wang, J. Lu, and J.-H. Jiang, Moderate-temperature near-field thermophotovoltaic systems with thin-film InSb cells, *Chin. Phys. Lett.* **38**, 024201 (2021).
- [46] Z. M. Zhang, *Nano/Microscale Heat Transfer* (McGraw-Hill, New York, 2007).
- [47] XiangLei Liu and YiMin Xuan, Super-Planckian thermal radiation enabled by hyperbolic surface phonon polaritons, *Sci. China Technol. Sci.* **59**, 1680 (2016).
- [48] Xiaohu Wu, Ceji Fu, and Zhuomin Zhang, Influence of hBN orientation on the near-field radiative heat transfer between graphene/hBN heterostructures, *J. Photonics Energy* **9**, 032702 (2018).
- [49] Xiaohu Wu and Ceji Fu, Near-field radiative heat transfer between uniaxial hyperbolic media: Role of volume and surface phonon polaritons, *J. Quant. Spectrosc. Radiat. Transfer* **258**, 107337 (2021).
- [50] Joshua D. Caldwell, Andrey V. Kretinin, Yiguo Chen, Vincenzo Giannini, Michael M. Fogler, Yan Francescato, Chase T. Ellis, Joseph G. Tischler, Colin R. Woods, and Alexander J. Giles, *et al.*, Sub-diffractive volumecnfined polaritons in the natural hyperbolic material hexagonal boron nitride, *Nat. Commun.* **5**, 1 (2014).
- [51] Siyuan Dai, Z. Fei, Q. Ma, A. S. Rodin, M. Wagner, A. S. McLeod, M. K. Liu, W. Gannett, W. Regan, and K. Watanabe, *et al.*, Tunable phonon polaritons in atomically thin van der Waals crystals of boron nitride, *Science* **343**, 1125 (2014).
- [52] Peining Li, Irene Dolado, Francisco Javier Alfaro-Mozaz, Félix Casanova, Luis E. Hueso, Song Liu, James H. Edgar, Alexey Y. Nikitin, Saül Vélez, and Rainer Hillenbrand, Infrared hyperbolic metasurface based on nanostructured van der Waals materials, *Science* **359**, 892 (2018).
- [53] Edward Yoxall, Martin Schnell, Alexey Y. Nikitin, Oihana Txoperena, Achim Woessner, Mark B. Lundeberg, Félix Casanova, Luis E. Hueso, Frank H. L. Koppens, and Rainer Hillenbrand, Direct observation of ultraslow hyperbolic polariton propagation with negative phase velocity, *Nat. Photonics* **9**, 674 (2015).
- [54] D. Polder and M. Van Hove, Theory of radiative heat transfer between closely spaced bodies, *Phys. Rev. B* **4**, 3303 (1971).
- [55] J. B. Pendry, Radiative exchange of heat between nanosstructures, *J. Phys.: Condens. Matter* **11**, 6621 (1999).

- [56] X. Wu, C. A. McEleney, M. González-Jiménez, and R. Macêdo, Emergent asymmetries and enhancement in the absorption of natural hyperbolic crystals, *Optica* **6**, 1478 (2019).
- [57] Z. Shi, M. González-Jiménez, X. Wu, C. A. McEleney, and R. Macedo, Asymmetric reflection induced in reciprocal hyperbolic materials, *ACS Photonics* **9**, 2774 (2022).
- [58] William Shockley and Hans J. Queisser, Detailed balance limit of efficiency of *p-n* junction solar cells, *J. Appl. Phys.* **32**, 510 (1961).
- [59] Mikyung Lim, Seokmin Jin, Seung S. Lee, and Bong Jae Lee, Graphene-assisted Si-InSb thermophotovoltaic system for low temperature applications, *Opt. Express* **23**, A240 (2015).
- [60] R. Messina and P. Ben-Abdallah, Graphene-based photovoltaic cells for near-field thermal energy conversion, *Sci. Rep.* **3**, 1383 (2013).
- [61] J.-H. Jiang and Y. Imry, Near-field three-terminal thermoelectric heat engine, *Phys. Rev. B* **97**, 125422 (2018).
- [62] M. G. Moharam, Drew A. Pommet, Eric B. Grann, and Thomas K. Gaylord, Stable implementation of the rigorous coupled-wave analysis for surface-relief gratings: Enhanced transmittance matrix approach, *J. Opt. Soc. Am. A* **12**, 1077 (1995).